Investigation of the Physical Aspects of Beta Imaging Probes Using Scintillating Fibers and Visible Light Photon Counters

L.R. MacDonald, M.P. Tornai*, C.S. Levin*, J. Park,
M. Atac, D.B. Cline and E.J. Hoffman*

Department of Physics, and *Division of Nuclear Medicine and Biophysics of the
Department of Molecular and Medical Pharmacology, and The Crump Institute for Biological Imaging
University of California, Los Angeles

Abstract

We are developing a hand-held imaging probe intended for intra-operative use. This probe is to be used after the bulk of a tumor has been removed. It will locate residual malignant tissue labeled by a pre-operative injection of a tumor-seeking radiopharmaceutical. The device presented here is a prototype system that consists of a 4 x 8 array of 925μm diameter plastic scintillating fibers. The imaging array is coupled to Visible Light Photon Counters (VLPCs) via 2 meters of optical fiber. We have obtained an intrinsic spatial resolution of < 1.0 mm with a highly collimated beta source, and a 2.0 mm resolution with a 1 mm, uncollimated source. Standard deviations of the relative gain and sensitivity over the 32 imaging elements were found to be 9.6% and 11.7% of the mean, respectively.

I. INTRODUCTION

The primary mass of a brain tumor is readily identified during surgery, but the boundaries, small extensions into normal tissue and small pieces of isolated tumor are difficult to determine precisely. The removal of residual tumor is very important to the recovery of the patient as even small amounts of tumor can lead to rapid reoccurrence of the disease [1-2]. It is equally important, and considerably more difficult in the brain, to avoid removing excess tissue that may be supporting vital functions. The current technique of multiple biopsies during surgery is time consuming and generally under-samples the tissue bed.

We are developing a hand held, imaging scintillation camera (imaging probe) to be used during surgery. The design goal is an imaging device that covers an area on the order of 1-2 cm^2 with intrinsic spatial resolution of the order of 1 mm. We focus on an imaging device because an imager can distinguish between concentrations of high activity and a large background in a single measurement. A single detector element (i.e. a non-imaging probe such as reference [3] with ~3 mm resolution) is too small to cover the entire tissue bed in a time compatible with surgery.

The probe will image distributions of radiopharmaceuticals that infiltrate the tumor at a significantly higher fraction than normal tissue. A promising candidate is ^{18}F-fluorodeoxyuridine (FDUR) which is reported to have a high tumor to tissue ratio [4-7]. This particular radiopharmaceutical allows diagnosis with PET to verify the location of the tumor and uptake of the FDUR. Then, during surgery, the imaging probe detects the positrons themselves instead of the 511 keV annihilation photons. This requires a detection system that is transparent to gamma radiation while remaining sensitive to betas. Due to the limited range of betas, only surface or near surface activity will be detectable. Because of this factor, the surgeon can be confident that the malignant tissue is near the surface and not another, deep lying source. In this work we investigate the properties of the scintillator, fiber optics, and photon detector that will influence the performance of an imaging probe.

II. PROTOTYPE IMAGING PROBE SYSTEM

A diagram of the system utilized for the measurements in this work is shown in Fig 1. Plastic scintillating fibers form the detector array, which are then coupled to clear optical fibers which are in turn coupled to Visible Light Photon Counters, or VLPCs.

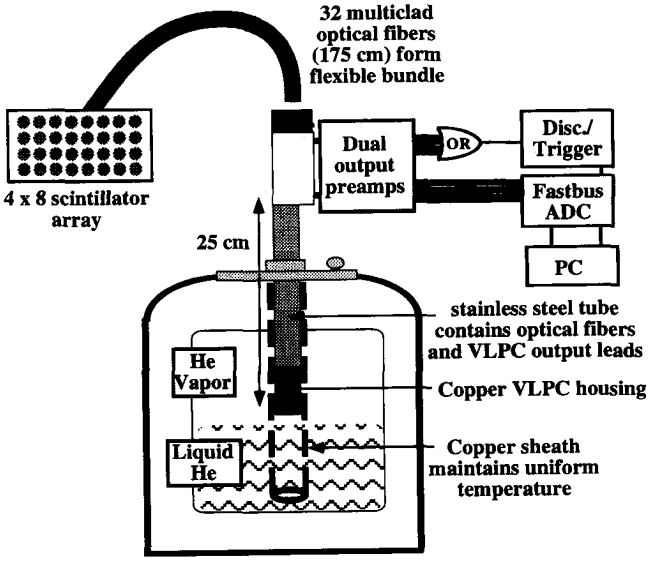

Figure 1. Components of the beta imaging intra-operative probe. A small liquid helium dewar is used to cool VLPCs which operate at about 7 degrees K in the vapor above the liquid.

0018-9499/95$4.00

A. Scintillating and Optical Fibers

The fiber optic bundle allows the concept to work by providing a light, flexible signal path to the relatively bulky VLPC dewar and electronics cabinet. In addition, the bundle isolates the surgical cavity from these electronics. However, because of significant light loss in coupling to fibers, the bundle also creates one of the major challenges of the technique. Over 30% of the photons produced in the scintillator can emerge for direct detection, but in our system one expects only about 2 to 7% of the scintillation photons to reach the other end of the fiber. The patient end of the fiber optic bundle is an optical coupler, which will allow a variety of imaging probes with specialized geometries to be used interchangeably during surgery.

The scintillating and clear fibers are multiclad (Kurary Corp.) in which the outer cladding is made of a fluorinated polymer with an index of refraction (n) equal to 1.42. The inner cladding is polymethylmethacrylate (PMMA) with n=1.49, and the core is polystyrene with n=1.59. The large difference in the n values of the outer clad and the core increases the amount of light trapped in the fiber, and the outer clad also acts as a protective coating, preventing surface imperfections and damage to the inner clad. The multiclad fibers have an 825 μm diameter core and two 25 μm thick claddings.

The imaging array of scintillators employed in this test system consists of a 4 by 8 set of 0.15% 3-hydroxyflavone (3HF) doped multiclad fibers. The 3HF fluorescence emission peaks near 535 nm. In a low density material such as polystyrene, positrons are readily absorbed, and the absorption of energy from 511 keV gammas is minimal (μ_γ=0.1 cm^{-1}). The scintillators are 2.5 cm long and the fiber centers are spaced by 1.27 mm. Each is thermally fused [8-9] to a 175 cm long, multiclad, clear fiber. A thin sheet of aluminized mylar covers the end of the scintillators not coupled to fibers. This reflector can, in principle, double the number of photons directed down the clear fiber. The attenuation length in the clear optical fibers is 7 - 8 m at 503 nm [10]. 32 of these fibers form a bundle that is then coupled to a 25 cm long set of fibers that extend to VLPCs (Fig 1). The experimental setup was created primarily from materials on hand and the results reported here are mainly proof of principle, not the evaluation of a functioning imaging probe. We are in the process of optimizing the system, initially by Monte Carlo simulation, which will guide our first attempts at optimized designs.

Using parameters from the cited literature we can estimate the fraction of photons created in the scintillator that reach the photodetector; a conservative trapping fraction in the multiclad scintillator is 5-10%; light transmission of the thermal fusing is between 80-90%, and attenuation losses in the 2 meters should be between 20-30%. The product of these factors (note that there are three couplings: 1) scintillator-optical fiber, 2) optical fibers at VLPC cassette, 3) fibers-VLPC) gives 1.8 - 5.8 % of the scintillation photons reaching the VLPC. An optical tracking Monte Carlo simulation (DETECT [11]) of this setup gave 6.8% photon transmission through the fibers. This matches the high end of the range calculated above when coupling to the VLPC is included. The calculated range is relatively conservative, so this result is reasonable. Conversion efficiency of the 3HF is about 6.6 photons per keV [12], thus, between 120 and 380 photons per MeV are likely to be incident on the VLPCs.

B. VLPCs

The photodetectors used were the latest version of VLPCs, designated HISTE-IV (Rockwell International Science Center) [10,13-15]. VLPCs are silicon-based solid state photon detectors with high quantum efficiency and large gain. At the emission wavelength of 3HF the quantum efficiency is between 60-70%. The VLPCs have a fast rise time (< 10 ns), operate continuously, have low power requirements (~1μW, -6.5 V operating voltage) and a gain of over 10^4. To achieve this sensitivity thermal noise must be suppressed by cooling to 7 degrees K. This is accomplished by operating the VLPCs in the vapor of a liquid helium dewar (Fig. 1).

Special cryostat cold-finger cassettes house the VLPCs. In our cassette, 4 linear arrays of 8 VLPCs, 1 mm in diameter each, are mounted in the cold-finger that will be inserted into a super-insulating dewar containing liquid helium. Fiber optics (Sect. II A) lead from the top of the cassette and are epoxied in position about 75μm from the surface of the VLPCs. Repeated tests have shown that thermal cycling of these fibers causes no ill effects. Fine leads carry the VLPC signal up and out of the cold-finger where connections to preamplifiers are made.

C. Data Acquisition Hardware

The VLPC signals are fed into fast, transimpedance preamplifiers (QPA02, [16]). The preamps have two output signals; one set goes to an analog OR circuit with the output delivered to a NIM discriminator. The discriminator supplies a trigger to a Fastbus ADC (LeCroy model 1885F) where the other set of preamp outputs is digitized (Fig. 1). The Fastbus is controlled with Lift3 software (LeCroy) on a PC.

III. SPECTRAL ANALYSIS

One of the difficulties in characterizing the imaging probe is the establishment of an energy calibration to allow a valid normalization of the gain and sensitivity of each element. The energy spectrum of a beta emitter is a continuum, therefore, there is no photopeak for setting up an energy window as with most gamma imaging devices in nuclear medicine.

A. Gamma Spectra

The probe is specifically designed to be insensitive to gamma rays, and attempting to detect even the Compton edge of several gamma sources for purposes of calibration proved difficult. A clear Compton edge was never seen and the resulting spectra were continua with few features. Figure 2 is a set of four spectra acquired with one of the probe's 32 fiber elements.

We analyzed the gamma spectra in two ways: (1) fit the region of the "Compton edges" to a Gaussian and compare centroids of different energy sources; (2) calculate weighted means of the spectra. The weighted mean calculation used the entire spectrum, excluding only electronic noise. The choice of lower channel threshold in the Gaussian fit method was more ambiguous. The only part of the gamma spectra that

might be expected to have a Gaussian shape is the usually sharp Compton edge that will smear because of the poor photon statistics of the system and/or incomplete energy deposition in the small scintillators. This can result in an asymmetric, semi-Gaussian shape. This analysis was very sensitive to the lower threshold chosen and to variations among the 32 individual imaging elements of the probe.

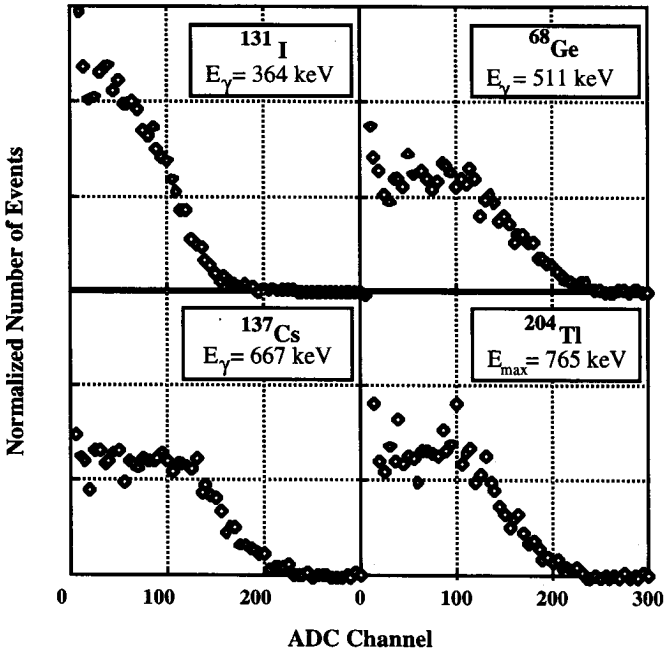

Figure 2. Spectra of 3 gamma sources and a beta source (^{204}Tl) acquired with channel 11 of the prototype beta-imaging intra-operative probe.

B. Beta Spectra

A traditional way of analyzing beta spectra is via a Kurie plot. The appendix treats the Fermi theory of beta decay and gives a brief explanation of a Kurie plot. In essence, a Kurie plot is a replot of a beta decay spectrum resulting in a straight line that intersects the energy axis at the endpoint energy (E_{max}) of the spectrum. Constructing a Kurie plot for each of the probe's channels gives a relative measure of each channel's gain.

With a more efficient scintillator-detector system we tested the application of a Kurie plot to an ^{18}F spectrum. Using a large (3" diameter, 0.2" thick) CaF_2(Eu) scintillating crystal coupled directly to a PMT, an ^{18}F spectrum was acquired and plotted with its associated Kurie plot (Fig. 3). The contribution of the 511 keV annihilation radiation has been subtracted from this spectrum, and the Kurie plot has been scaled to the y-axis of the spectrum. Superimposed is the theoretical spectrum (see the appendix); slight deviations are seen at high energies probably due to remaining background contribution. The Kurie plot is linear over a large region, deviating only at the extremes, as does the spectrum. The Kurie plot can thus provide a standard by which to evaluate the beta spectra; E_{max} extracted from the fits can be normalized for each element of the imager, and possibly compared with the known source spectrum for depth of source information [17].

The same analysis is shown in Fig. 4 for a ^{204}Tl spectrum collected with one of the probe's 32 scintillating fibers. ^{204}Tl is a long lived β^- emitter with E_{max} = 765 keV. The long half-life (3.8 yrs) of ^{204}Tl makes this a convenient calibration source, and its energy is in the range for which we are designing the probe. Fig. 4b is the Kurie plot associated with the spectrum of Fig. 4a, and is fit to a line over the region that the spectrum is seen to agree with theory .

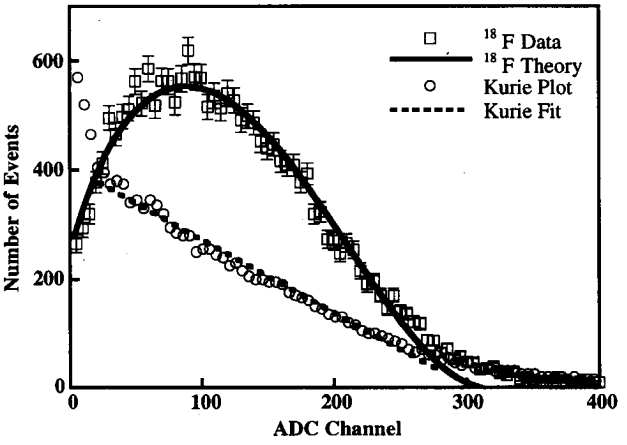

Figure 3. The spectrum of ^{18}F collected with a CaF_2(Eu) crystal on a PMT is plotted with the theoretical prediction (see appendix). Open circles are the Kurie plot of this spectrum. A linear fit to the region where the spectrum matches theory can be extrapolated to the horizontal axis to ascertain the endpoint energy (E_{max}) of the spectrum.

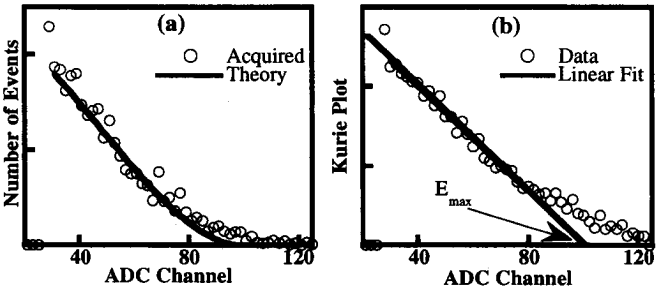

Figure 4. (a) A ^{204}Tl spectrum collected with fiber 12 of the probe. The acquired spectrum follows theory well from electronic noise to ADC channel 80. (b) The Kurie plot of the spectrum shown in (a) is fit with a line up to channel 80, then extrapolated to find E_{max}.

The problems encountered with this technique were rooted in its reliance on the analytical expression for the spectral shape. Deviations from the theoretical spectral shape cause distortions in the Kurie plot, complicating this analysis. Distortions can result from a number of factors: 1) contamination from 511 keV annihilation gammas; 2) the small size of the scintillators may result in incomplete energy deposition; 3) absorption of positron energy in surrounding scatter material.

The weighted mean technique outlined in Section III A. is also applicable to the beta spectrum.

IV. CALIBRATION

A. Gain and Sensitivity

The result of the gain and sensitivity calibrations using the methods described above can be seen in Fig. 5. Both Kurie plot and weighted mean methods were used to calculate the gain variations for a ^{204}Tl flood irradiation. In Fig. 5a these two measurements are normalized to one another. Weighted mean and Gaussian fit analyses of gamma sources (^{131}I, ^{68}Ge-Ga, ^{137}Cs and ^{60}Co) showed similar variations. The Kurie plot method yielded the smallest standard deviation, 9.6% of the mean. The weighted mean technique gave similar results; standard deviations ranged from 9%-12%.

To measure the sensitivity variation we corrected the sensitivity calculations by the gain variations found in Fig. 5a. The gain corrected sensitivity is displayed in Fig 5b.

The dead channels seen in Fig. 5 have subsequently been reduced from five to three channels. One bad channel is a poor/broken thermal fuse between scintillator and optical fiber. Another is a noisy preamp, and the third is a weak VLPC or bad connection.

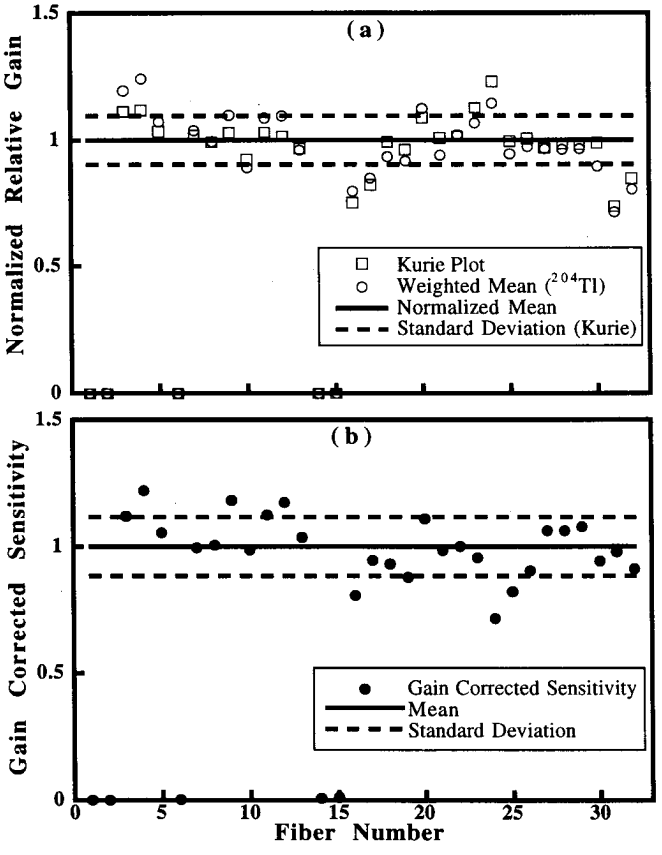

Figure 5. (a) Gain variation of the 32 element probe. Normalized results from both Kurie plot and weighted mean analyses for ^{204}Tl are seen. (b) Gain corrected sensitivities of the individual fiber elements. Five dead channels are seen on the x-axes.

B. Energy Calibration

Spectral analysis techniques of Sect. III A were used to calculate the relationship between source energy and Fastbus ADC channel. Ideally, this relationship would be linear, but because of the small size of the scintillators, non-linearity was anticipated and found. A monotonic increase in ADC channel was seen with increasing source energy, but consistently leveled off at higher energies.

C. Monte Carlo Simulations

To understand the energy calibration result, we used Monte Carlo simulations to model beta and gamma interactions in the scintillators. The Monte Carlo code EGS4 was used to model the energy deposition from the various sources in the scintillators. The Monte Carlo showed the scintillators to absorb energy from only 13%-18% of the incident gammas, depending on source energy. The simulated beta source (^{204}Tl) showed energy deposition for 80% of the events. Energy deposition simulated for small scintillators did show a defined Compton edge for low energy sources (Fig. 6). Compton electrons can scatter without full energy deposition, but because of the length of the scintillators (2.5 cm), electrons from photon scattering near 180^{o} can be fully absorbed, producing a sharp Compton edge. However, at the energy of ^{60}Co (gammas at 1.2 & 1.3 MeV) even the Compton edge disappears. The typical plateau region below the Compton edge is not seen in Fig. 6. As the finite resolution of the system blurs the spectrum, it becomes difficult to identify the location of the Compton edge (Fig. 2).

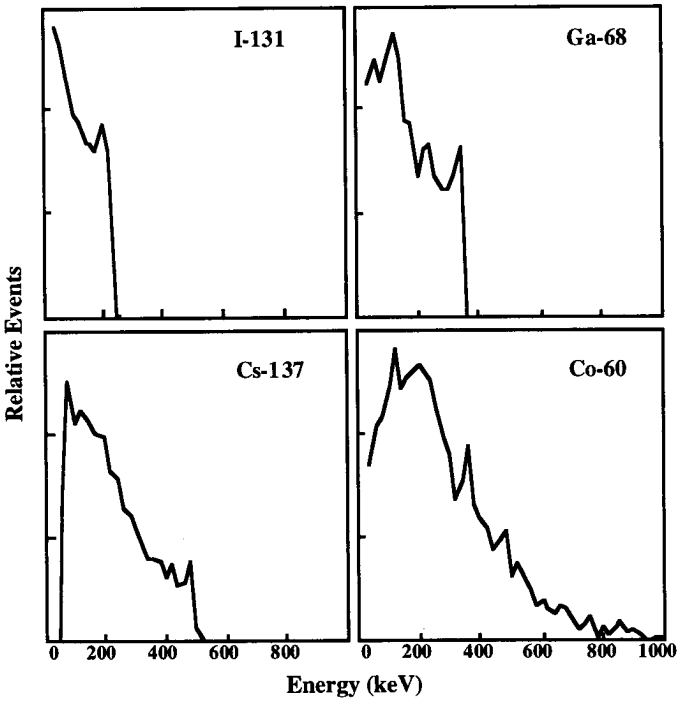

Figure 6. Simulated energy deposition from the indicated sources in the scintillating fibers of the probe, i.e. the best spectra the probe could produce. Compton edges are visible for the lower energy sources, but not for ^{60}Co which emits gammas at 1170 & 1330 keV.

In Section II A a rough calculation showed between 120-380 photons/MeV incident on the VLPCs. If we assume a 60% VLPC quantum efficiency, we can expect (assuming Poisson statistics) an energy resolution of no better than 15-25% FWHM at 1 MeV (Fig. 7a). Simulations with larger resolution (~50% FWHM at 1 MeV) were found to more accurately match the data. This type of simulated spectrum is shown in Fig. 7b, superimposed on data acquired with the probe.

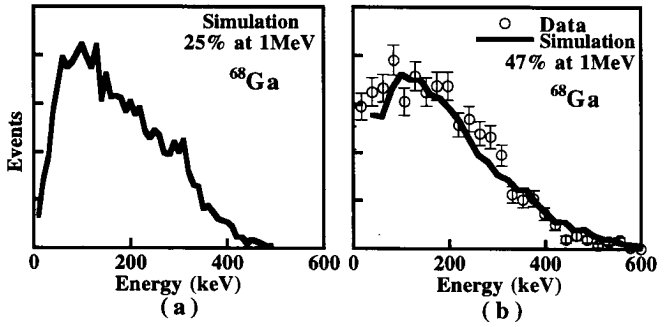

Figure 7. (a) An energy resolution 25% FWHM at 1 MeV, a best case calculation using just photon statistics, was incorporated into the ^{68}Ge-Ga spectrum of Fig. 6 to produce the spectrum shown here. (b) With 47% FWHM at 1 MeV the simulation better reproduces the data. The Compton edge is no longer discernible.

V. SPATIAL RESOLUTION

Spatial resolution was measured with both collimated and uncollimated ^{204}Tl beta sources. The scintillating fibers have a higher sensitivity to beta particles than gamma-rays. Betas are also much easier to collimate. Point spread functions of the probe are shown in Fig. 8. This measurement was made with a 0.5 mm line source scanned across the scintillating array. Fig. 8 shows one of the rows of scintillators after correction for gain and sensitivity. The central six fibers are displayed.

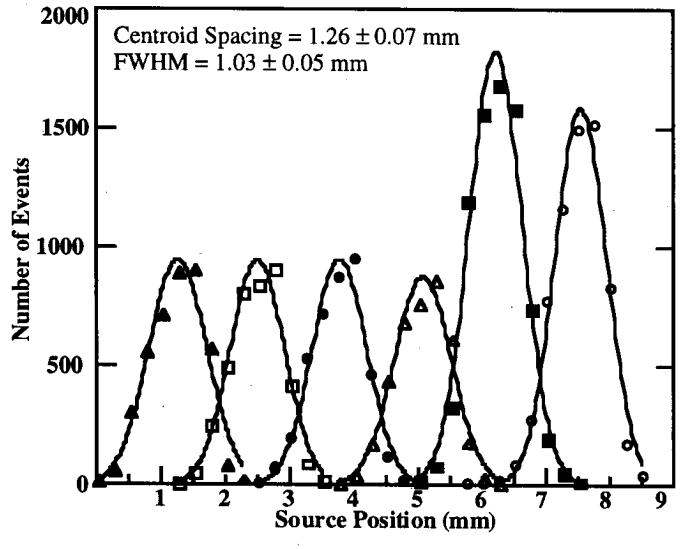

Figure 8. Point spread function of probe. Mean FWHM and centroid spacing are indicated. Error bars on these data are the size of the data points.

Individual peaks are fit to Gaussians, the mean full width half maximum (FWHM) is 1.03 ± 0.05 mm and the mean spacing between centroids is 1.26 ± 0.07 mm. The scintillators and source are of comparable size, a deconvolution of the source size would give a FWHM closer to the 0.925 mm diameter of the scintillators.

With a 1.0 mm diameter pencil beam of forward directed betas we can consistently detect a signal in exclusively one of the probe's 32 scintillators. The basic response of the probe to this source arrangement is shown in Fig. 9. Each lego block represents one of the scintillating fibers (dead channels in black). This response is nearly a delta function, i.e. non-zero only at the irradiated fiber. A two dimensional Gaussian fit to this data gives FWHM = 1.28 mm in both dimensions which, within error, is the center to center spacing of the scintillators.

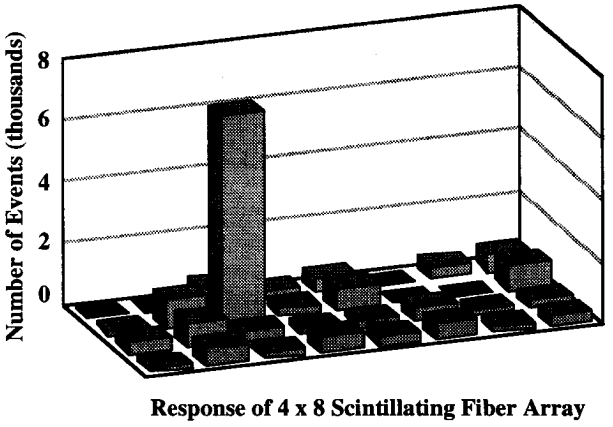

Figure 9. Probe response to collimated beta source. 925 μm diameter fibers, center spaced 1.27 mm, are represented by square pixels here. Dead space is depicted and dead channels are black.

The type of source that will be seen in clinical use is simulated by a source that is 1 mm in extent but uncollimated, thus betas are emerging in a 2π sr solid angle. This source causes a response in several fibers. The FWHMs of 2-D Gaussian fits range from 1.8 to 2.2 mm depending on the relative location of dead spaces with respect to the source.

In order to better define the spatial response of the system, data were acquired in four positions to create a single well sampled image. The four positions formed a square and were separated by one half the center-to-center fiber spacing. By moving the probe one half pixel steps we fill the dead space area. This technique was applied to the two point sources described above. Fig. 10 shows the results of the fine sampling measurement. These results are equivalent to the measurement of the intrinsic resolution for a scintillation camera (Fig. 10a,b), and the image resolution (Fig. 10c,d)

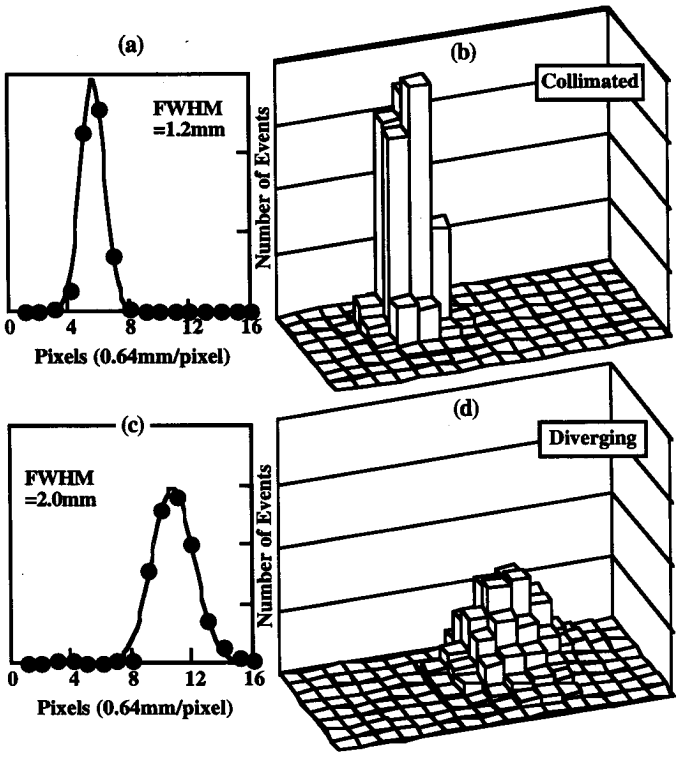

Figure 10. Interleaving technique fills dead space. More finely sampled sources are: (a) & (b) the forward-directed 1mm collimated source; (c) & (d) 1mm uncollimated diverging source. In (b) & (d) the number of events are normalized and 4 boxes are equivalent to one fiber of the probe. In (a) & (c) cuts from (b) & (d), respectively, are fit to Gaussians. Full width half maximum are given.

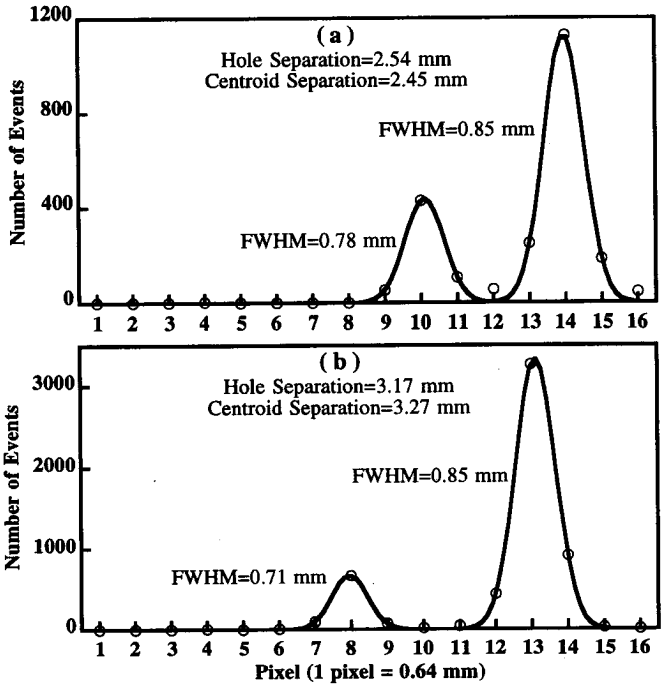

Figure 11. (a) Two 0.5 mm pencil beams of ^{204}Tl betas. Centers of the beams are separated by 2.54 mm. Parameters of a fit to the sum of two Gaussians are given. (b) Centers of the 0.5 mm diameter beams separated by 3.17 mm.

Finally, the over sampling technique was applied to two sets of double pinholes. The pinholes were 0.5 mm in diameter and spaced by 3.17 mm in one set (Fig. 11b), and 2.54 mm in the other (Fig. 11a). Fig. 11 displays the resolution of the probe to these sets of pinholes. Here we see that with the very small pinholes the intrinsic resolution is less than 1 mm FWHM.

VI. CONCLUSION

This preliminary investigation of the physical aspects of a potential intra-operative imaging probe has provided generally positive results. The combination of double clad optical fibers and VLPCs, as the photon detector, provide a signal that is well above the noise and shows a response that is sensitive enough to the input energy to provide a modest level of energy discrimination. The uniformity of signal gain and sensitivity among the elements was reasonable (~ 10 %). The intrinsic resolution of the elements was on the order of 1 mm, while the resultant image resolution for uncollimated betas was on the order of 2 mm. This means the resolution is not limited by the detector but by the properties of the source.

The system tested here is pre-prototype. Further optimizations, both obvious (scintillator packing fraction), and subtle (scintillator geometry, surface treatment, reflector), should provide significant improvement over the device described here.

ACKNOWLEDGMENTS

The authors thank Claudio H. Rivetta of FERMILAB for technical assistance. This work was funded in part by DOE Contract DE-FC03-87-ER60615 and NCI grant R01-CA61037.

REFERENCES

[1] P. Black and S. Ronner, "Cortical Mapping for Defining the Limits of Tumor Resection", Neurosurgery, vol. 20, No. 6, pp. 914-919, 1987.

[2] P. Black, "I. Brain Tumors, Medical Progress-Review Article", New Eng J Med, vol. 324, No. 21, pp.1471-1476, 1991.

[3] F. Daghighian *et al.*, "Intraoperative Beta Probe: A Device for Detecting Tissue Labeled Intraoperatively with Positron or Electron Emitting Isotopes During Surgery", Med Phys, vol. 21, No. 1, pp. 153-157, 1994.

[4] Y. Abe *et al.*, "Tumor Uptakes of ^{18}F-5-Fluorouracil, ^{18}F-5-Fluorouridine, ^{18}F-5-Fluorodeoxyuridine in Animals", Eur J Nuc Med, vol. 8, pp.258-261, 1983.

[5] K. Ishiwata *et al.*, "II. Metabolic Investigation of ^{18}F-5-Fluorouracil, ^{18}F-5-Fluoro-2'-deoxyuridine and ^{18}F-5-Fluorouridine in Rats", Eur J Nuc Med, vol. 9, pp.185-189, 1984.

[6] K. Ishiwata *et al.*, "Metabolic fates of ^{18}F-5-Fluoro-2'-deoxyuridine in Tumor Bearing Mice and Human Plasma", Nuc Med Biol, vol. 18, pp. 539-545, 1991.

[7] S. Starosta-Rubinstein *et al.*, "Imaging of a Glioma Using Peripheral Benzodiazepine Receptor Ligands", Proc Natl Acad Sci USA, vol. 84, pp. 891-895, 1987.
[8] M. Atac, W.Foster and M. Lundin, Fermilab Pub-537, 1990.
[9] G. Apollinari, D. Scepanovic and S. White, "Plastic Optical Fiber Splicing by Thermal Fusion", NIM A311, pp.520-528, 1992.
[10] B. Baumbaugh *et al.*, "Performance of Multiclad Scintillating and Clear Waveguide Fibers Read Out with Visible Light Photon Counters", NIM A345, pp. 271-278, 1994.
[11] G.F. Knoll *et al.*, "Light Collection in Scintillation Detector Composites for Neutron Detection", IEEE Trans Nuc Sci NS-35 (1), pp. 872-875, 1988.
[12] A. Bross *et al.*, "Radiation Effects in Intrinsic 3HF Scintillators", NIM A327, pp.337-345, 1993.
[13] M.D. Petroff and M.G. Stapelbroek, "Photon Counting Solid-State Photomultiplier", IEEE Trans Nuc Sci NS-36 (1) pp.158-162, 1989.
[14] M.D. Petroff and M. Atac, "High Energy Particle Tracking Using Scintillating Fibers and Solid State Photomultipliers", IEEE Trans Nuc Sci NS-36 (1), pp. 163, 1989.
[15] M. Atac *et al.*, "Scintillating Fiber Tracking for the SSC Using Visible Light Photon Counters", NIM A314, No. 1, pp. 56-62, 1992.
[16] T. Zimmerman, "A High Speed, Low Noise ASIC Preamplifier for Silicon Strip Detectors", IEEE Trans Nuc Sci NS-37 (2), pp. 439-443, 1990.
[17] T. Baltakmens, "A Simple Method for Determining the Maximum Energy of Beta Emitters by Absorption Measurements", NIM vol. 82, pp. 264-268, 1970.
[18] H. Daniel, "Shapes of Beta-Ray Spectra", Rev Mod Phys, vol. 40, pp.659-672, 1968.
[19] C.S. Wu, S.A. Moszkowski, *Beta Decay*, Interscience Publishers, 1966.
[20] I. Feister, "Numerical Evaluation of the Fermi Beta-Distribution Function", Phys Rev, vol. 78, pp.375-377, 1950.

APPENDIX: Fermi Theory of Beta Decay

In beta decay, beta rays are emitted with a continuous distribution of energies up to a maximum (E_{max}) equal to the amount of energy liberated in the decay. When the energy of the beta ray is less than E_{max} the remaining energy of the decay is carried off by a neutrino.

There are a number of different classifications of beta decay and variations in the shape of the spectra. A general formula for the energy distribution is of the form [18,19];

$$N(E)dE = g\, F(Z,E)\, p\, E\, (E_{max}-E)^2\, dE \qquad (1)$$

N(E) =number of decays at energy E (g is a coupling constant)
E = total β energy in units of its rest mass energy,
E_{max} = maximum β energy (in units of rest mass),
p = momentum of β in units of mc,
F(Z,E) = Fermi function, Z=atomic number of decay daughter.

The Fermi function represents the Coulomb interaction between the beta and the daughter nucleus.

A Kurie plot is a graph of $(N / g\, F\, p\, E)^{1/2}$ vs. E, which results in a straight line that intersects the E-axis at the endpoint energy, E_{max}.

A nonrelativistic approximation for F(Z,E) is valid for *allowed* transitions, generally lighter elements. ^{18}F is an allowed transition. *Forbidden* transitions, such as ^{204}Tl, require a more sophisticated calculation of F(Z,E). The nonrelativistic Fermi function is [19]

$$F_{allow}(Z,E) = 2\pi\eta / (1 - e^{-2\pi\eta}) \qquad (2)$$

with $\eta = \mp Z\alpha E/p$ for $\beta^{\pm}$ decay, $\alpha=1/137$, the other variables are defined above. The approximation used for ^{204}Tl is the nonrelativistic Fermi function multiplied by additional factors [20];

$$F_{forbid} = F_{allow}(Z,E)\, p^{2S}\, (\eta^2+1/4)^S \qquad (3)$$

where $S = (1-(Z\alpha)^2)^{1/2} - 1$, is a constant.

These are the results used to analyze the beta ray spectra presented in this work.